



Extremely Slow ($V_{\text{sw}} < 300 \text{ km s}^{-1}$) Solar Winds (ESSWs) at 1 au: Causes of Extreme Geomagnetic Quiet at Earth

Bruce T. Tsurutani¹ and Rajkumar Hajra² ¹ Retired, Pasadena, CA, USA; bruce.tsurutani@gmail.com² Indian Institute of Technology Indore, Simrol, Indore 453552, India

Received 2022 March 5; revised 2022 May 19; accepted 2022 May 20; published 2022 September 9

Abstract

A search for extremely slow ($V_{\text{sw}} < 300 \text{ km s}^{-1}$) solar winds (ESSWs) at 1 au has been conducted using hourly average solar wind data from 1963 through 2021. 297 ESSW events were identified with an average duration of $\sim 2.0 \pm 1.4$ days. The lowest speed detected was 156 km s^{-1} . Ten of the lowest-speed events were analyzed in detail. It was found that all 10 events were located at the ends of high-speed solar wind (HSSW) streams. The termination of the ESSWs was caused by high-density plasmas, either a corotating interaction region associated with the next HSSW stream or a heliospheric plasma sheet encounter. There was a greater occurrence of ESSW events in solar cycles 23 and 24 than in previous solar cycles. This phenomenon is associated with the much lower solar activity during these two cycles. The decrease in solar polar open magnetic fields was accompanied by an increase in low and midlatitude open magnetic fields. The ESSWs were accompanied by low interplanetary magnetic fields ($4.4 \pm 2.1 \text{ nT}$) and low negative interplanetary B_z fields ($-1.7 \pm 1.5 \text{ nT}$), which led to extreme geomagnetic quiet: $AE = 67 \pm 78 \text{ nT}$ and $Dst = 2.2 \pm 9.9 \text{ nT}$. We encourage magnetospheric researchers to use ESSW events to better understand the ground states of the magnetosphere and ionosphere.

Unified Astronomy Thesaurus concepts: Solar wind (1534); Slow solar wind (1873); Solar coronal mass ejections (310); Geomagnetic fields (646)

Supporting material: figure sets, machine-readable table

1. Introduction

In the Neugebauer & Snyder (1966) paper, they discovered “streams of hot, high-velocity plasma that recurred at 27 day intervals with a peak velocity of 830 km s^{-1} and a peak (proton) temperature of $9 \times 10^5 \text{ K}$. Between streams the velocity dropped to as low as 307 km s^{-1} with a temperature of $3 \times 10^4 \text{ K}$.” After the peak velocities in the high-speed streams were reached, the velocities decreased slowly until they asymptotically obtained their minimum values. Thus, all values in between the peak speed and the minimum speed were detected.

Belcher & Davis (1971) in another epic paper found that “the purest examples of outward propagating Alfvén waves occurred in high-velocity streams and on their trailing edges (where the velocity decreases with time).” Their Figure 13 presented their idea of why the high-speed streams decreased gradually after the peak values: rarefaction/super-radial expansion. The term *super-radial expansion* is used to mean where the plasma does not strictly go radially outward, but expands in the directions away from radial. Belcher & Davis (1971) found that the “low velocity regions have smaller amplitude Alfvén waves and tend to be less pure in the sense that they are more strongly intermixed with structures of a non-Alfvénic and possibly static nature.”

The above two papers (and many others since then) defined the two types of solar winds as we know them today, the high-speed solar wind (HSSW) and slow solar wind (SSW) (the names have changed slightly with time). The HSSW is now

known to originate at solar coronal holes (Krieger et al. 1973) and has peak speeds (V_{sw}) of $\sim 750\text{--}800 \text{ km s}^{-1}$ (Phillips et al. 1995; Tsurutani et al. 2006a). Coronal holes are a dominant solar feature of the solar cycle declining phase and solar minimum. Two prominently related types of geomagnetic activity at Earth associated with HSSWs are high-intensity long-duration continuous auroral electrojet (AE) activities (HILDCAAs: Tsurutani & Gonzalez 1987; Kozyra et al. 2006; Hajra et al. 2013) and magnetospheric relativistic electron acceleration (Hajra et al. 2015; Hajra & Tsurutani 2018a). HILDCAAs are now known to be a combination of substorms (Akasofu 1964) and DP2 (Nishida 1968) events (Tsurutani et al. 2004a).

The SSW has been defined as having $V_{\text{sw}} \sim 350\text{--}450 \text{ km s}^{-1}$ at 1 au (see recent review by Abbo et al. (2016) and references therein). One possible solar source originates at or near solar helmet streamers (Gosling et al. 1981; Suess et al. 2009) in the form of discrete plasma blobs (Sheeley et al. 2009). A possible mechanism is interchange reconnection at streamer cusps (Fisk & Schwadron 2001; Wang et al. 2012). Several other scenarios for the SSW have been discussed in Abbo et al. (2016). At 1 au, the heliospheric current sheet (HCS; Smith et al. 1978) is a typical feature of the SSW of this type (see schematic in Tsurutani et al. 2006a). The high plasma densities adjacent to the HCS, called the heliospheric plasma sheet (HPS; Winterhalter et al. 1994), when impacting the Earth’s magnetosphere, causes compression of the magnetosphere and sudden and drastic loss of magnetospheric relativistic electrons (Tsurutani et al. 2016; Hajra & Tsurutani 2018a).

D’Amicis & Bruno (2015) (see also D’Amicis et al. 2021) have found another type of SSW that has a strong Alfvénic wave component. This is significantly different than the SSW that Belcher & Davis (1971) studied, and was discussed above.



Original content from this work may be used under the terms of the [Creative Commons Attribution 4.0 licence](https://creativecommons.org/licenses/by/4.0/). Any further distribution of this work must maintain attribution to the author(s) and the title of the work, journal citation and DOI.

Tsurutani & Gonzalez (1987) and Tsurutani et al. (1995, 2011b) studied the Alfvénicity of the trailing portion of HSSW streams. They found that although the Alfvénicity remained high, the amplitude of both the interplanetary magnetic field (IMF) magnitude and the B_z component decreased with decreasing velocity. Tsurutani et al. (2011a) studied the causes of the all-time minimum of the geomagnetic ap index in 2008–2009 and found that it was due to HSSW streams that had peak speeds less than 500 km s^{-1} . The latter authors concluded that these low-peak speeds were due to super-radial expansion of HSSWs coming from midlatitude coronal holes.

Sanchez-Diaz et al. (2016) studied what they called the *very slow solar wind* (VSSW) with speed less than 300 km s^{-1} detected by the Helios spacecraft from 0.3–0.7 au. Sanchez-Diaz et al. found that the events “usually contained the heliospheric plasma sheet and heliospheric current sheet.” From this, Sanchez-Diaz et al. “suggest that VSSW events may be the interplanetary signatures of long HPS crossings.” Their modeling predicted that VSSW events would not survive to distances 1 au from the Sun and beyond.

Not included in the above solar wind characterization are interplanetary coronal mass ejections (ICMEs). Fast ($V_{\text{sw}} > 500 \text{ km s}^{-1}$) ICMEs are generally associated with solar flares and disappearing filaments (Sheeley et al. 1976; Tang et al. 1989). These events occur predominantly during solar maximum and a few years after the maximum. ICMEs are impulsive with variable peak speeds at 1 au ranging from $\sim 400 \text{ km s}^{-1}$ to as high as $> 2000 \text{ km s}^{-1}$ for the 1859 Carrington event (Carrington 1859; Cliver et al. 1990; Tsurutani et al. 2003). After the ICME peak speeds are reached, their velocities decrease very much like HSSW streams. Tsurutani & Lakhina (2014) have suggested that ICME speeds of $\sim 2700 \text{ km s}^{-1}$ at 1 au are possible under the right solar wind conditions. These fast ICMEs and their upstream sheaths are responsible for superstorms at Earth (Tsurutani et al. 1992; Echer et al. 2008; Lakhina et al. 2012; Meng et al. 2019). An extreme event of this type is the Carrington magnetic storm (Carrington 1859; Chapman & Bartels 1940; Tsurutani et al. 2003; Lakhina & Tsurutani 2018).

Slow ICMEs ($V_{\text{sw}} \sim 350\text{--}400 \text{ km s}^{-1}$) are thought to have been accelerated by the SSW from their initially slow speeds ($V_{\text{sw}} < 350 \text{ km s}^{-1}$) near the Sun. A subset of these may be associated with magnetic reconnection at the edges of coronal holes (Chen 2011). These small-size ICMEs have been detected at 1 au and have been noted to cause fairly intense geomagnetic storms (Tsurutani et al. 2004b). However, because these ICMEs are *slow*, they do not have leading shocks and sheaths and therefore in these cases the IMF southward components (B_s) within the magnetic clouds are causing the storms through magnetic reconnection.

Lacking in the above discussion is the question, do solar winds with speeds less than 300 km s^{-1} (which we call here *extremely slow solar winds* or ESSWs) exist at 1 au and if so, what are their geomagnetic effects? What are the solar or interplanetary causes of these streams? To address this issue, we will examine solar wind data at 1 au from 1963–2021 to identify possible intervals of $V_{\text{sw}} < 300 \text{ km s}^{-1}$ and if found, to determine their related geomagnetic effects at Earth. It will be shown that there are many extended intervals of ESSW events detected at 1 au, contrary to the conclusions of Sanchez-Diaz

et al. (2016). The ESSW events will be shown to occur particularly frequently more recently in solar cycles 23 and 24.

2. Data and Method of Analyses

The interplanetary data at 1 au from 1963 November 27 to 2021 September 24 were obtained from the NASA OMNI data center (https://spdf.gsfc.nasa.gov/pub/data/omni/low_res_omni/). Both 1 hr and 1 minute average data were used for this study. This interplanetary data set is a compilation of data from a variety of satellites taken over many years. The data has been shifted (in time) to take into account the solar wind propagation delay from the satellite location to the Earth’s bow shock nose. The IMF data are given in a geocentric solar magnetospheric (GSM) coordinate system.

The solar wind ion charge state ratios C6+/C5+ and O7+/O6+ at 1 au are obtained from measurements by the Solar Wind Ion Composition Spectrometer (SWICS) instrument on board the Advanced Composition Explorer (ACE; <http://www.srl.caltech.edu/ACE/ASC/level2/index.html>). The ion charge state data will be used to identify HSSW streams coming from solar coronal holes. High ion charge state ratios indicate a coronal hole source (e.g., von Steiger 1996; von Steiger et al. 2000).

The Ulysses solar wind data at $\sim 2 \text{ au}$ were obtained from COHWeb (<https://omniweb.gsfc.nasa.gov/coho/>). The polar coronal hole locations and extents were obtained from the National Solar Observatory homepage (<http://solis.nso.edu/vsm/>). The north pole data will be shown to illustrate the small variability in solar wind velocity from a coronal hole.

The geomagnetic activity indices, AE and Dst have been obtained from the World Data Center for Geomagnetism, Kyoto, Japan (<http://wdc.kugi.kyoto-u.ac.jp/>). The 1 hr Dst index is composed of four near-equatorial ground magnetometer observatory data and can be used to identify magnetic storm ring current activity. The 1 hr AE index, a proxy for the auroral ionospheric electrojet current, is composed of 12 auroral zone ground magnetometer observatories and can be used to identify auroral zone substorm activity. AE data are not available after 2017. Thus, we have also used SME data (1 minute) available at SuperMAG (<https://supermag.jhuapl.edu/>; Gjerloev 2009) to extend the study in time. The SME data are based on ~ 300 ground-based magnetometers and give much finer spatial scale resolution plus sub-auroral latitudinal coverage.

The daily $F_{10.7}$ solar flux was obtained from the Laboratory for Atmospheric and Space Physics (LASP) Interactive Solar Irradiance Data Center (<https://lasp.colorado.edu/lisird/>). This data will be used to identify solar cycle phases.

HSSW streams are typically identified by fast rises to a maximum of $\sim 750\text{--}800 \text{ km s}^{-1}$ with a long slow decay (Tsurutani et al. 1995, 2005a). It should be noted that during the solar minimum phase that occurred after solar cycle 23 (SC23) the peak HSSW speeds only reached $\sim 500 \text{ km s}^{-1}$ (Tsurutani et al. 2011b). This will be discussed later in this paper.

Corotating interaction regions (CIRs) form at the antisolar edges of HSSW streams where the HSSWs overtake the upstream SSWs (Belcher & Davis 1971; Smith & Wolfe 1976; Tsurutani et al. 1995). In the approximate center of a CIR is a discontinuity called a stream interface. The stream interface separates the compressed SSW material (the antisolar side of the CIR) from the compressed HSSW material (the solar side of

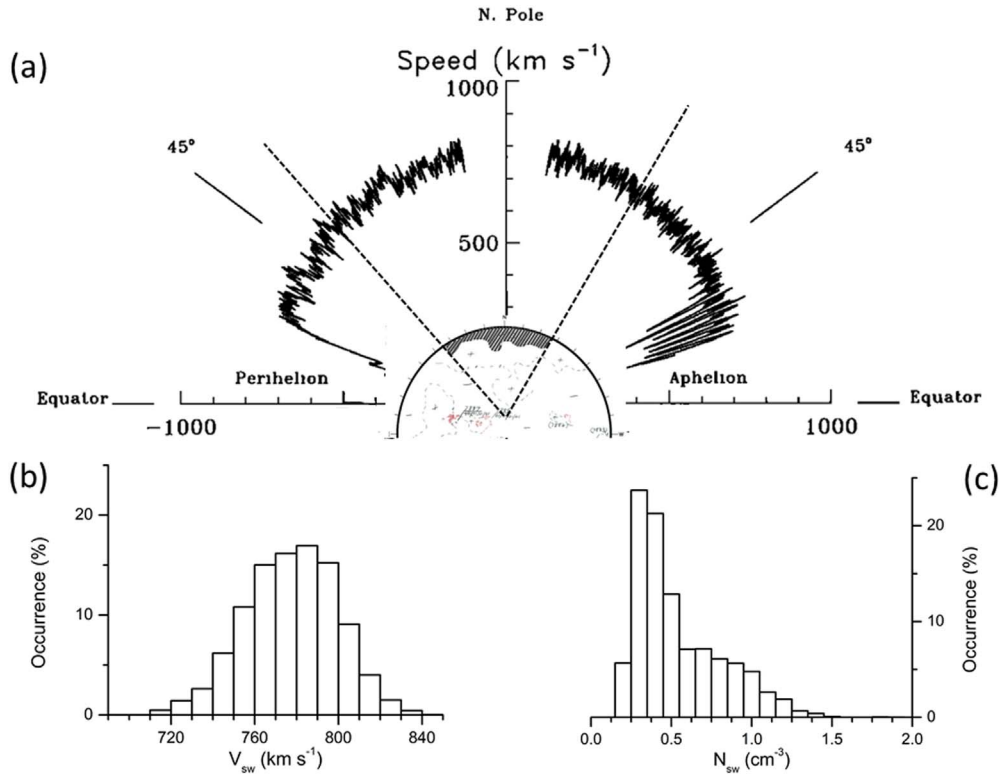


Figure 1. The solar wind velocities at high solar latitudes obtained by Ulysses at ~ 2 au from the Sun. On the top (a), the solar wind velocities are given by the radial extent of the plot from the center of the figure (a dial plot). The polar coronal hole area is indicated in the figure of the Sun. Two dashed lines indicate the radial extent of the northern polar coronal hole. On the bottom are histograms of (b) the velocities and (c) densities for the interval over the solar north pole between the two radial dashed lines. Panel (a) is adapted from McComas et al. (2000).

the CIR). A CIR is essentially a double sheath containing high plasma densities and high magnetic field magnitudes.

The HCS (Smith et al. 1978) is a feature of the SSW. The HCS is believed to be an interplanetary extension of the tips of solar helmet streamers. Crossings of the HCS at 1 au can be identified in the IMF data by a reversal in the B_x and B_y components. HCSs (and stream interfaces) are tangential discontinuities. Other interplanetary discontinuities such as fast magnetosonic shocks and their identification methods are discussed in Tsurutani et al. (2011c).

To determine the Alfvénicity of the solar wind, we follow the Belcher & Davis (1971) technique where a cross correlation between a component of IMF and a component of V_{sw} is calculated. For this study, we have used the z component. To simplify the plots, the absolute values of the correlation coefficient are used (the signs of the correlation coefficients give an indication of wave propagation direction, information not used in this study).

3. Results

To start the discussion of the ESSW at 1 au, we first show the velocity distribution of the solar wind emanated from a large coronal hole over the solar north pole. What is important is the maximum speed and the variability of the speeds. These properties will be compared to the Neugebauer & Snyder (1966) results to give context to this paper. To do this, the best example to use is Ulysses data taken over the solar pole at a distance of ~ 2 au. Figure 1 shows the high latitude Ulysses solar wind velocities over its first northern polar pass. The large polar coronal hole (with positive magnetic polarity) area taken on day 185 in 1995 is indicated at the top of Figure 1(a).

Dashed radial lines indicate the latitudinal extent of this coronal hole. The interval between the two lines occurred on days 123–365 in 1995. If the HSSW came purely radially outward, the HSSW would be confined to the region of latitudes between the two lines. However, it can be noted that the latitudinal extent of the HSSW is essentially double the latitudinal extent subtended by the two lines.

Histograms of both the solar wind velocity (V_{sw}) and proton density (N_{sw}) are shown at the bottom of Figure 1. V_{sw} ranged from a minimum value of ~ 698 km s $^{-1}$ to a maximum value of ~ 841 km s $^{-1}$, with a mean value of ~ 777 km s $^{-1}$. Note the maximum Ulysses value is close to the value quoted by Neugebauer & Snyder (1966) in their first observation of the HSSW measured at 1 au. This range of speeds shown in the histogram fits well with the values of ~ 750 – 800 km s $^{-1}$ used by researchers in describing the typical peak speeds in HSSW events. The density has an average value of 0.54 cm $^{-3}$ with a minimum value of 0.16 and a maximum value of 1.91 cm $^{-3}$. The low-density numbers are due to radial expansion of the solar wind.

Figure 2 gives an overview of the solar wind data and the corresponding geomagnetic activity for the entire period of study (1963–2021). The top panel (a) shows the range of the solar wind velocities as a function of time. Solar wind cases with $V_{sw} < 300$ km s $^{-1}$ are indicated in red and cases where $V_{sw} \geq 300$ km s $^{-1}$ are indicated in black. The data for the entire study interval are separated into those hourly averages where $V_{sw} < 300$ and ≥ 300 km s $^{-1}$. Panels (b)–(g) show the solar wind parameters and geomagnetic activity indices for $V_{sw} < 300$ km s $^{-1}$ in red and $V_{sw} \geq 300$ km s $^{-1}$ in black. Panel (h) gives the $F_{10.7}$ flux in blue and the number of ESSW events in black histogram format.

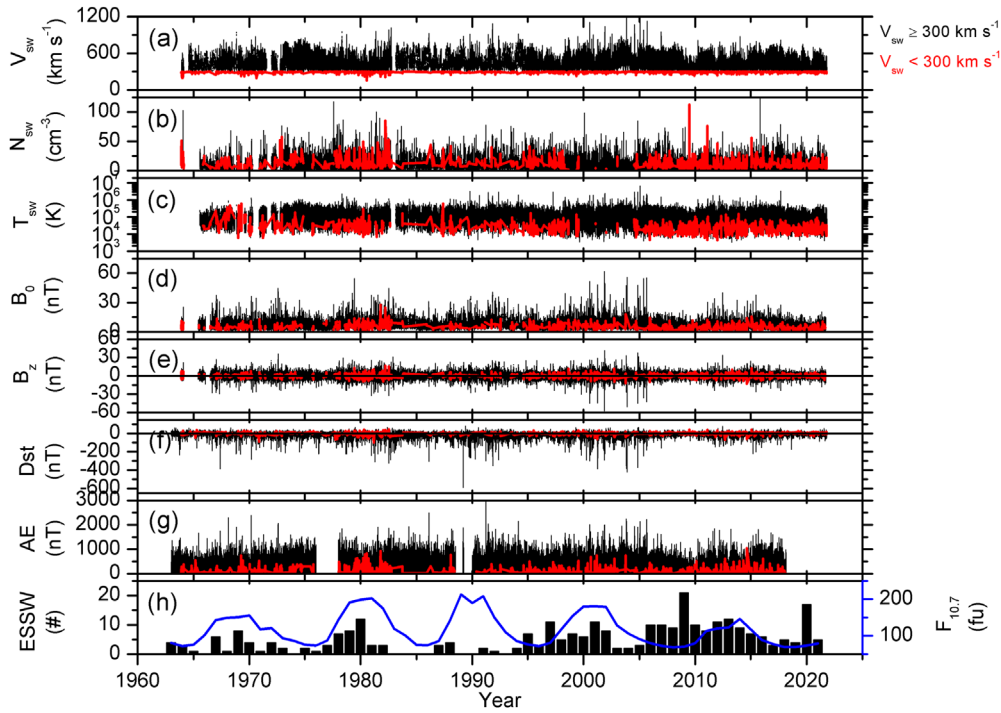


Figure 2. The ranges of solar wind parameters and geomagnetic activity indices from 1963–2021. From top to bottom are the temporal variations of the ranges of (a) the solar wind velocity (V_{sw}), (b) the proton density (N_{sw}), (c) the proton temperature (T_{sw}), (d) the IMF magnitude (B_0), (e) the z component of the IMF (B_z), (f) the Dst index, and (g) the AE index. Panel (h) gives the number of ESSW events (black histograms, scale on the left) and the $F_{10.7}$ solar flux (blue, scale on the right). For panels (a)–(g), all of the solar wind and geomagnetic activity data with $V_{sw} < 300 \text{ km s}^{-1}$ are shown in red and $V_{sw} \geq 300 \text{ km s}^{-1}$ are shown in black.

The solar wind density N_{sw} (panel (b)) for the ESSW cases is typically not the lowest and can occasionally be the highest for particular times. Cases of the latter can be seen in 1982 and 2009. The solar wind proton temperature T_{sw} (panel (c)) is almost always near the minimum value. This is particularly noted in the interval of 2005–2021. However, exceptions to this can be found in 1963–1970.

The ESSW IMF magnitude B_0 (panel (d)) is generally on the relatively low side. Again, this is most apparent from 2005–2021. An exception to this can be noted in 1983 where there are high B_0 values. The ESSW B_z values (panel (e)) are also low with the exception of the 1983 interval.

The Dst index (panel (f)) for ESSW events is generally not very negative. It should be noted that there are more positive values than negative values of Dst for the ESSW cases. This may be due to sudden impulses (SI^+ s) caused by relatively high solar wind densities compressing the magnetosphere. The AE index (panel (g)) indicates that auroral zone geomagnetic activity during ESSWs is generally low, but there are exceptions. Several exceptions can be noted in the 1979–1980 and 1982 intervals.

Perhaps the most striking data is contained in the bottom panel (panel (h)). It shows that the ESSW events occur during all phases of the solar cycle. They can occur during solar maximum (1969, 1980, 2001, 2013) and during solar minimum (1975, 1995, 2009, 2020). Perhaps even more striking is the large number of ESSW events during 2006–2020. In this interval, there seems to be little or no solar cycle dependence at all. There are two peak occurrences, one in 2009 and another in 2020. These two specific time intervals will be revisited later.

Figure 3 gives a quantitative description of solar wind and the geomagnetic activity parameters taken over the 58 yr study interval. The figure shows the distribution of values for the

hourly averages of the solar wind and geomagnetic activity parameters. In panel (a), the ESSW events are indicated by red. In the following panels (b)–(g), the black curves correspond to the distribution of values for all solar wind and geomagnetic activity observations, while the ESSW events are indicated in red. The distributions are summarized in Table 1. In the table, the statistical probability factor or the p -value is estimated based on the mean values and standard deviations of each parameter for all solar winds and ESSW streams. The p -value less than 0.05 indicates that the two means are significantly different (Press et al. 1992). Thus, from the table, we can conclude that all the parameters have significantly different values during ESSWs than during all solar winds.

Table 1 gives the quantitative values for the parameters shown in Figure 3. Consistent with Figure 2, the average N_{sw} (Figure 2(b)) for the ESSW intervals is $10.7 \pm 6.6 \text{ cm}^{-3}$ compared with $6.7 \pm 5.4 \text{ cm}^{-3}$ for all solar winds. The ESSW average T_{sw} is $2.3 \times 10^4 \text{ K}$ in comparison to $1.0 \times 10^5 \text{ K}$ for all solar winds. It is noted that the temperature range for the ESSW intervals is at the very low end of the proton temperature range (Figure 3(c)). The IMF B_0 average is $4.4 \pm 2.1 \text{ nT}$ for the ESSW events whereas the average is $6.1 \pm 4.1 \text{ nT}$ for all solar wind intervals. The IMF negative B_z average is $-1.7 \pm 1.5 \text{ nT}$ for the ESSW events while the IMF negative B_z average is $-2.2 \pm 2.2 \text{ nT}$ for all solar wind intervals.

For the ESSW events, the Dst values have a range between $+46 \text{ nT}$ and -62 nT with an average of $+2 \pm 10 \text{ nT}$. The former is due to possible high solar wind density pressure compressing the magnetosphere and the latter is due to one very small magnetic storm ($\text{Dst} \leq -50 \text{ nT}$; Gonzalez et al. 1994). This was the only ESSW geomagnetic storm during the ~ 58 yr of survey. The Dst distribution in Figure 3(f) indicates that the distribution is quite narrow. The AE values for ESSW

Table 1
Distribution Functions of the Solar Wind Parameters

	All Solar Wind				ESSW Events				<i>p</i> -value
	Min	Max	Mean	Median	Min	Max	Mean	Median	
V_{sw} (km s ⁻¹)	156	1189	433 ± 102	410	156	299	285 ± 13	288	<0.0001
N_{sw} (cm ⁻³)	0.3	137	6.7 ± 5.4	5.2	0.4	112.3	10.7 ± 6.6	9.3	<0.0001
P_{sw} (nPa)	0.03	76.06	2.25 ± 1.85	1.81	0.05	12.93	1.58 ± 0.98	1.37	<0.0001
T_{sw} (10 ⁴ K)	0.3	663.2	10.2 ± 9.7	7.3	0.4	49.0	2.3 ± 1.8	1.9	<0.0001
B_0 (nT)	0.4	62.0	6.1 ± 3.1	5.4	0.5	24.8	4.4 ± 2.1	4.0	<0.0001
B_z (nT)	-57.8	+41.6	-0.01 ± 3.11	0.0	-13.1	+16.3	+0.04 ± 2.28	0.0	0.0929
Dst (nT)	-589	+81	-14 ± 22	-10	-62	+46	+2 ± 10	+3	<0.0001
AE (nT)	3	3195	200 ± 206	120	3	1052	67 ± 78	42	<0.0001

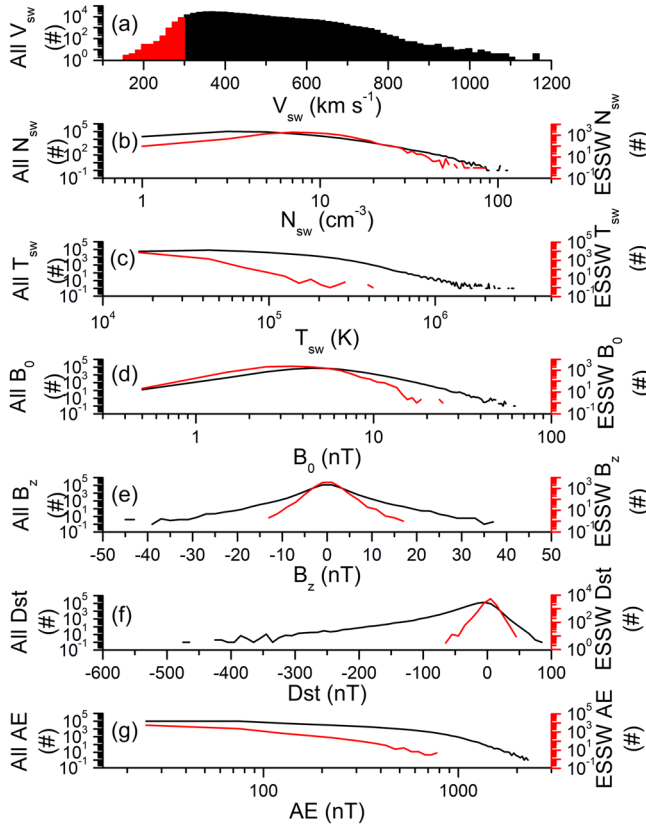


Figure 3. Distributions of solar wind and geomagnetic activity parameters for the $V_{sw} < 300$ km s⁻¹ (ESSW) intervals (in red) and for all solar winds with $V_{sw} < 300$ and ≥ 300 km s⁻¹ (in black) for the entire study interval for panels (b)–(g). In panel (a) the all interval is both the red and black areas. The scales for the distributions of the parameters for ESSW events are given on the right. The scales for the distributions of all parameters for the whole interval of the study are given in the left margins.

intervals are extremely low, 67 ± 78 nT. These geomagnetic index values indicate extreme geomagnetic quiet conditions.

There were 297 ESSW intervals found in this study. A list of all events is given in the [Supporting Information](#). From Figure 3 (and Table 1), the minimum hourly V_{sw} value of all ESSW intervals of this study is 156 km s⁻¹. This occurred at ~03:00 UT on day 204 of 1980. To examine the ESSW intervals further, we have examined the 10 lowest solar wind speed events in detail. Four of such intervals are shown in Figures 4 and 6.

Figure 4 shows two ESSW events occurring during 2009. The intervals are indicated by gray vertical shadings. Panel (a)

gives the solar wind velocity V_{sw} where a horizontal red line indicates the threshold of 300 km s⁻¹ used in this study.

The first ESSW interval can be noted to be the trailing part of an HSSW. The HSSW event had a peak speed of 458 km s⁻¹ at ~20:00 UT on day 328. The HSSW is characterized by high ion charge state ratios: C6+/C5+ and O7+/O6+. The charge state ratios are particularly high in the ESSW interval. The Alfvénicity index (absolute value of the cross correlation between B_z and V_z) is high throughout the entire HSSW and perhaps slightly lower in the ESSW interval. The whole HSSW was ~10.9 days long including the ESSW interval.

The first ESSW interval occurred between days 334 and 339. The ESSW interval is ~5.2 days long. This event had a minimum speed of 233 km s⁻¹ at 06:00 UT on day 339.

The Dst value is mostly small and positive throughout the first ESSW interval. A peak Dst of +18 nT at ~07:00 UT on day 339 occurred with the impingement of the high-density region onto the magnetosphere at the end of the ESSW interval.

The second ESSW event in Figure 4 lasts from ~14:00 UT on day 343 to ~07:00 UT on day 350, or a duration of 6.7 days (this ESSW event may actually be two events). This event is again located in a trailing portion of an HSSW stream. The peak speed of the HSSW stream was 418 km s⁻¹ at ~06:00 UT on day 340. The second ESSW event had a minimum solar wind speed of 251 km s⁻¹ at ~04:00 UT on day 346. Two HCS crossings are detected at ~17:00 UT on day 346, and at ~06:00 UT on day 348. An HPS associated with the first HCS crossing had a broad density increase of 17.5 cm⁻³ which caused a Dst increase to +19 nT. The second HCS crossing had a density spike of 26.7 cm⁻³ which caused a SI⁺ of ~0 nT and triggered a small substorm of AE = 356 nT. The second ESSW event was terminated by a third HSSW event. This HSSW event reached a maximum speed of 437 km s⁻¹ at ~10:00 UT on day 352. Unlike the first ESSW interval, this second ESSW interval showed lower C6+/C5+ and O7+/O6+ charge state ratios. The Alfvénicity of the second ESSW interval was as high as the rest of the HSSW interval.

Figure 5 shows a blow-up of the high-density region at the end of the first ESSW interval of Figure 4. One minute average solar wind data are used. The high plasma density of ~28 cm⁻³ is noted from ~06:00 to ~19:00 UT on day 339.

There are three new unidentified discontinuities associated with the high-density region. These are indicated by vertical dashed lines. The first one occurs at ~06:35 UT on day 339. At this discontinuity, V_{sw} increases from 237 to 261 km s⁻¹, N_{sw} increases from ~12 to 29 cm⁻³, and T_{sw} increases from 0.86×10^4 to 1.41×10^4 K. The IMF B_0 remains approximately unchanged across this discontinuity. This is not a forward

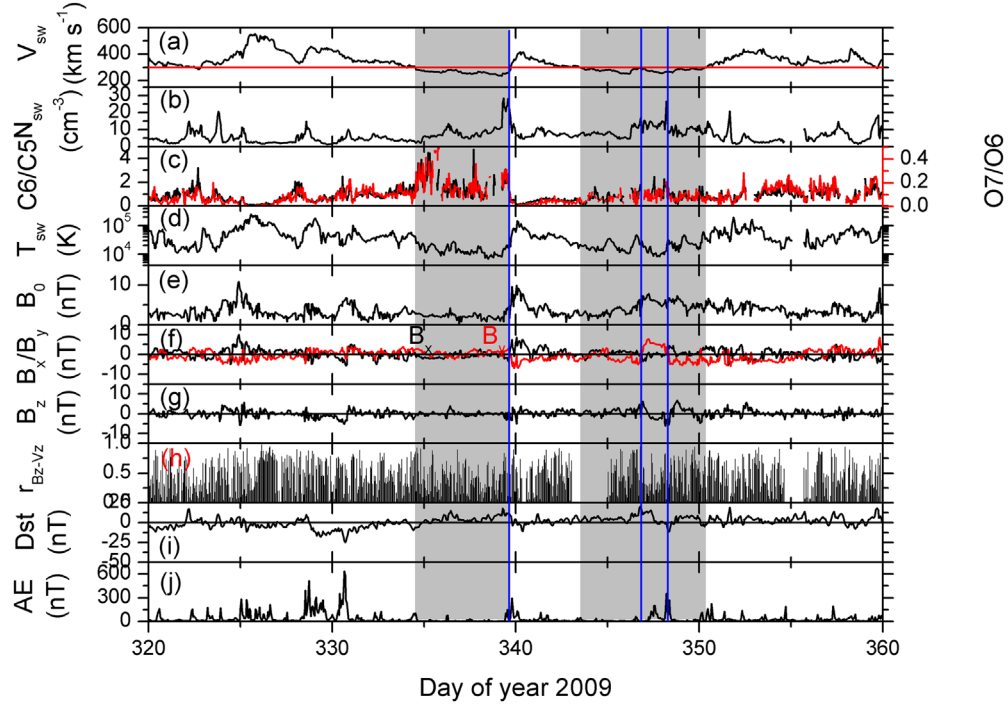


Figure 4. Two ESSW events identified on days 334–339 and days 343–350 in 2009. The panels from top to bottom are (a) V_{sw} (km s^{-1}), (b) N_{sw} (cm^{-3}), (c) carbon and oxygen ion charge state ratios in the same panel, (d) T_{sw} (K), (e) IMF B_0 (nT), (f) B_x/B_y (nT), (g) B_z (nT), (h) B_z-V_z correlation coefficient, (i) Dst (nT), and (j) AE (nT). The red horizontal line in panel (a) corresponds to $V_{sw} = 300 \text{ km s}^{-1}$. The two ESSW events are indicated by vertical shadings. Blue vertical lines indicate HCS crossings.

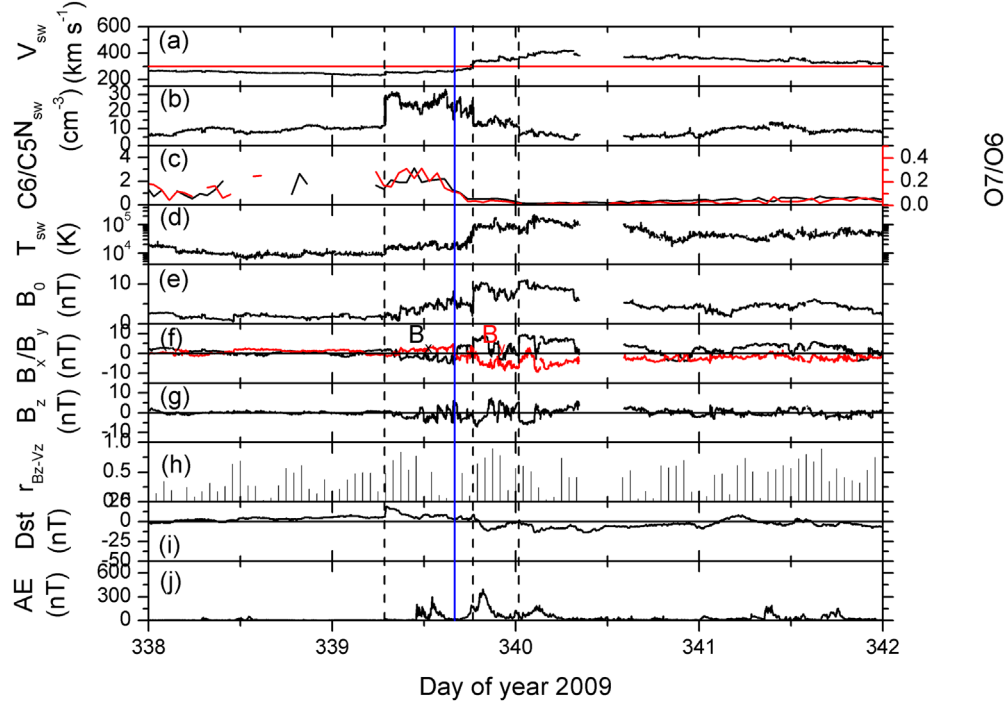


Figure 5. One minute average solar wind data for the high-density region ending the first ESSW event shown in Figure 4. The panels are in the same format as in Figure 4. Black vertical dashed lines indicate interplanetary discontinuities (other than HCS crossings).

shock. The second discontinuity at $\sim 18:22$ UT on day 339 has a V_{sw} increase from ~ 279 to 335 km s^{-1} , N_{sw} a decrease from ~ 25 to 12 cm^{-3} , T_{sw} increased from 2.4×10^4 to $9.7 \times 10^4 \text{ K}$, and B_0 increase from ~ 2.6 to 8.6 nT . What is very striking about this second discontinuity is that it terminates the high C6 +/C5+ and O7+/O6+ ion charge state ratio region. The third,

small discontinuity is located at $\sim 00:01$ UT on day 340. There is an N_{sw} decrease from ~ 11.0 to 6.0 cm^{-3} , and a small B_0 increase from 8.9 to 10.6 nT . There are also sharp changes in the B_y and B_z components at this discontinuity.

It is suggested that this high magnetic field magnitude and high-density structure is a CIR created by the HSSW interval

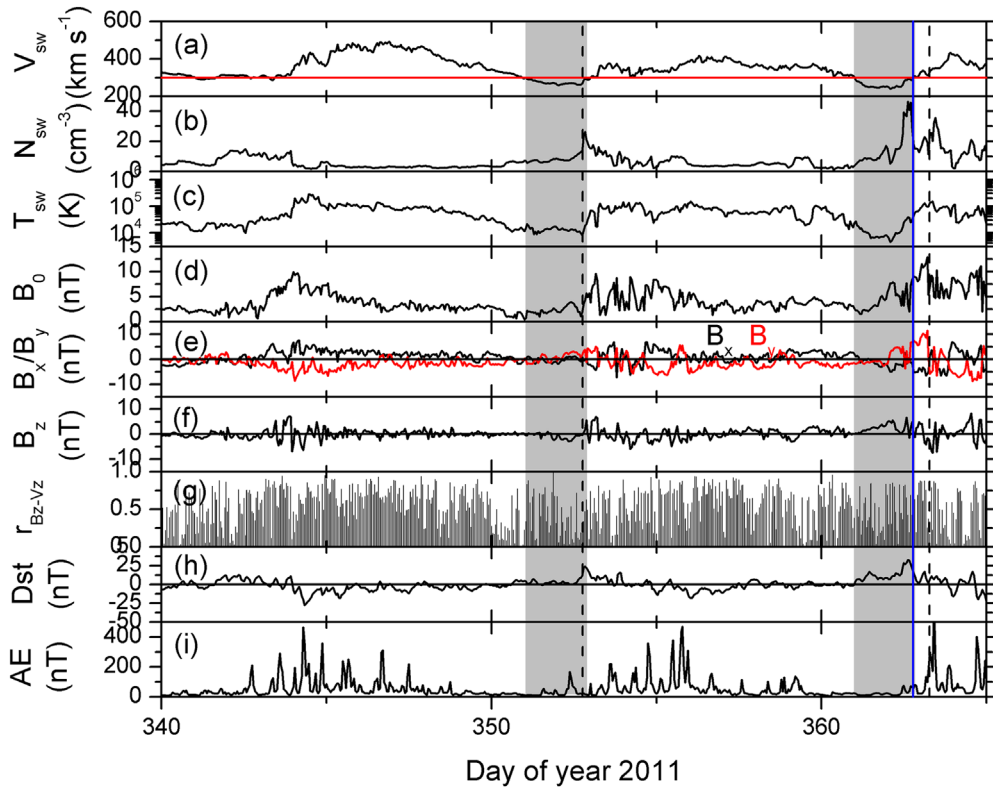


Figure 6. Two ESSW events found on days 351–352 and days 360–362 in 2009. The panels from top to bottom are (a) V_{sw} (km s^{-1}), (b) N_{sw} (cm^{-3}), (c) T_{sw} (K), (d) IMF B_0 (nT), (e) B_x/B_y (nT), (f) B_z (nT), (g) B_z-V_z correlation coefficient, (h) Dst (nT), and (i) AE (nT). The two ESSW events are indicated by vertical shadings. Ion charge state ratios were unavailable for this interval.

that follows. The center discontinuity is the stream interface separating the antisunward, compressed trailing portion of the ESSW from the sunward portion of the oncoming HSSW interval. The first and third discontinuities bounding the CIR are not fast shocks. They have been tested and do not fit shock properties.

The sunward side of the CIR is compressing the SSW, which is the trailing portion of the HSSW! This is consistent with the findings of D’Amicis et al. (2021) and explains their general results of SSWs with high Alfvénicities. The ESSW is the extreme trailing portion of the HSSW. To our knowledge, this is the first CIR that has been reported in the SSW and certainly the first reported in the ESSW.

The vertical blue line is an HCS as was previously indicated in Figure 4. HCSs are typically embedded in CIRs at 1 au (Tsurutani et al. 1995). CIRs typically form forward and reverse shocks at distances beyond 1 au from the Sun (Smith & Wolfe 1976). These observations are consistent with the high-density region terminating the ESSW event as being a CIR.

Figure 6 shows two more ESSW events, one from $\sim 01:00$ UT on day 351 to $\sim 21:00$ UT on day 352 (~ 1.8 days long), and the second from $\sim 00:00$ UT on day 361 to $\sim 20:00$ UT on day 362 (~ 1.8 days long). The minimum speed of the first event is 259 km s^{-1} and 240 km s^{-1} for the second event.

The first event is associated with the extreme end of an HSSW stream. The peak speed of the stream was 491 km s^{-1} at $\sim 21:00$ UT on day 346. The high Alfvénicity throughout the HSSW is apparent, as shown in panel (h). The Alfvénicity is slightly less in the ESSW region. The first ESSW event is ended by a high plasma density interval.

The second ESSW event occurs at the end of what appears to be several smaller streams. The maximum speed of 419 km s^{-1} occurred at $\sim 07:00$ UT on day 356. The smaller streams are characterized by high Alfvénicity. The ESSW interval is Alfvénic but slightly smaller than in the main portion of the streams. The second ESSW event is terminated by a high-density region with peak density of 46.5 cm^{-3} at $\sim 15:00$ UT on day 362. The details of this will be discussed in the following higher resolution figure. This causes a Dst increase of $+33 \text{ nT}$.

The AE values of the two ESSW events are low. AE ranges from ~ 10 to $\sim 168 \text{ nT}$ for the first event and from ~ 10 to $\sim 81 \text{ nT}$ for the second event. Other than the two high Dst values associated with the high plasma densities that terminate the two ESSW events, the ranges of Dst for the first event are from $+1$ to $+24 \text{ nT}$, and from $+1$ to $+33 \text{ nT}$ for the second event.

Figure 7 shows the high solar wind density structure that terminates the second ESSW interval shown in Figure 6. One minute average solar wind data are used. The peak density of $\sim 60 \text{ cm}^{-3}$ occurs at $\sim 12:56$ UT on day 362 within the ESSW interval. The compression of the magnetosphere creates a peak Dst of $+31 \text{ nT}$.

The nature of this density structure is not obvious. The lack of charge state ratios makes it difficult to conclude. There are no clear major discontinuities as was the case for the event shown in Figure 5. One small discontinuity is present at $\sim 10:16$ UT on day 362. At that discontinuity, N_{sw} increases from ~ 19 to 33 cm^{-3} , T_{sw} increases from 1.2×10^4 to $2.1 \times 10^4 \text{ K}$ and B_0 increases from 3.1 to 7.6 nT . V_{sw} increased only slightly across this discontinuity, from ~ 253 to 272 km s^{-1} . The discontinuity did not fit the properties of a fast forward shock.

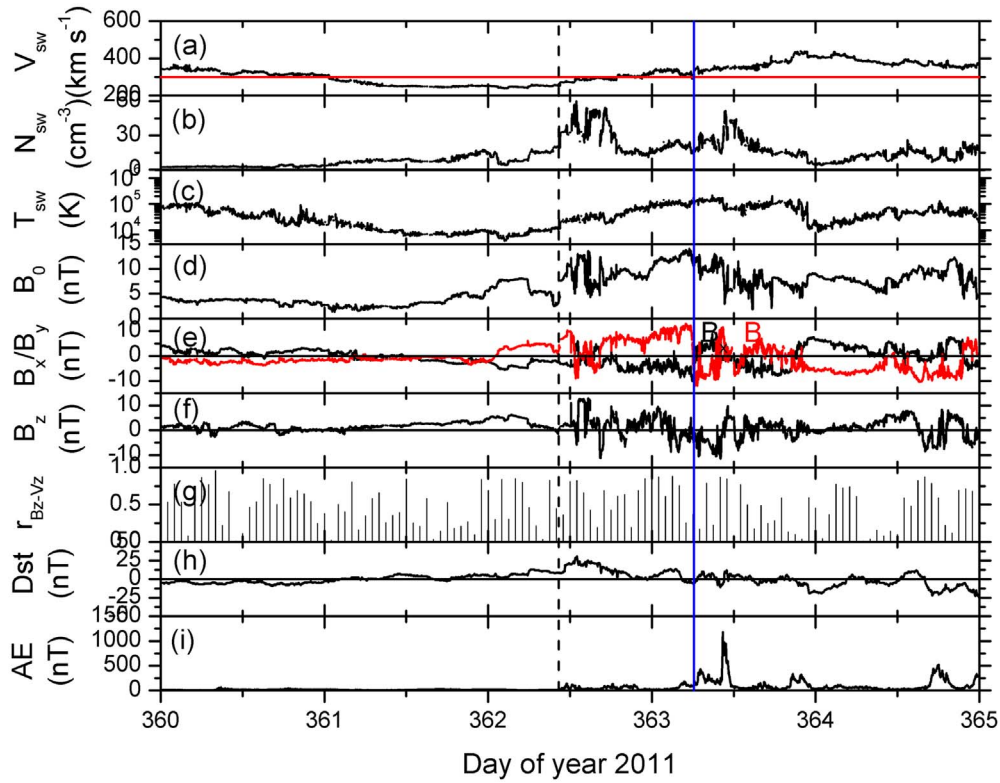


Figure 7. The format is the same as in Figure 5 (except ion charge state ratios were unavailable). One minute average solar wind data are used to study the high-density region that terminates the second ESSW interval shown in Figure 6.

At $\sim 06:03$ UT on day 363 there is a reversal between the IMF B_x and B_y signs. B_x changes from negative values to positive values. B_y does the reverse. This is an HCS. One possible interpretation of this high-density region is that it is a CIR at its formative stage.

The 10 lowest-speed ESSW events have been plotted in the same format as Figures 4 and 6 and are shown in Appendix A. The results from their analyses are essentially the same as in Figures 4 and 6. The ESSW events occur at the extreme ends of HSSW events. They have high Alfvénicity and generally high C6+/C5+ and O7+/O6+ ion ratios. The ESSW events are terminated by high plasma density intervals, either a CIR or an HPS. The Alfvénicity of the ESSW events generally is slightly lower than in the HSS proper.

3.1. The Solar Wind During Solar Minimum Intervals: 2009 and 2020

In Figure 2 it was shown that there were maxima in ESSW event occurrences in 2009 and 2020. Figure 8 shows those two intervals in more detail. The left-hand panel for 2009 shows that the interval contained many HSSW events. The maximum peak velocity of the HSSW events in 2009 was ~ 688 km s $^{-1}$. This occurred on day 58. Note that the peak velocity never reached the values noted in Neugebauer & Snyder (1966) or in the Ulysses survey shown in Figure 1.

Dividing the 2009 interval into halves, the average solar wind V_{sw} was ~ 373 and ~ 355 km s $^{-1}$, respectively. The number of ESSW events were 10 and 11, respectively. The average Dst was -3 and -2 nT, respectively. The average AE was 76 and 63 nT, respectively. As the peak values of the HSSW events decreased, so did the Dst and AE values, while the number of ESSW events remained essentially the same.

This general feature was previously noted in greater detail in Tsurutani et al. (2011b).

The right-hand panel shows the year 2020. The peak speed (~ 701 km s $^{-1}$ on day 217) never reached the range of ~ 750 – 800 km s $^{-1}$. The interval is again filled by many HSSW intervals. The ESSW events are found at the extreme ends of HSSW events (not shown).

The decrease in the peak V_{sw} values of the HSSW events has been suggested to be due to super-radial expansion from small coronal holes located at midlatitudes on the Sun (De Toma 2011; Tsurutani et al. 2011b).

3.2. ESSW Events During Solar Maxima: 2001 and 2013

It can be noted from Figure 2 that many ESSW events occurred during solar maxima, especially in SC23 and SC24. To determine if some different phenomena were causing the ESSW events, the years 2001 and 2013 were studied. Appendix B shows plots of the solar wind and geomagnetic activity indices for both of these years. To summarize our findings, we did not find any ESSW intervals associated with ICMEs or their trailing edges. These 2001 and 2013 ESSW intervals were found to occur in HSSW extreme ends, similar to what was shown in Figures 4 and 6, and the rest of the 10 lowest velocity ESSW events shown in Appendix A.

4. Summary and Conclusions

We have searched the solar wind data during 1963–2021 at 1 au for ESSW intervals where $V_{sw} < 300$ km s $^{-1}$. Two hundred and ninety-seven ESSW intervals were identified (see Supporting Information). The average length of the ESSW intervals was $\sim 2.0 \pm 1.4$ days. The average IMF B_0 of the

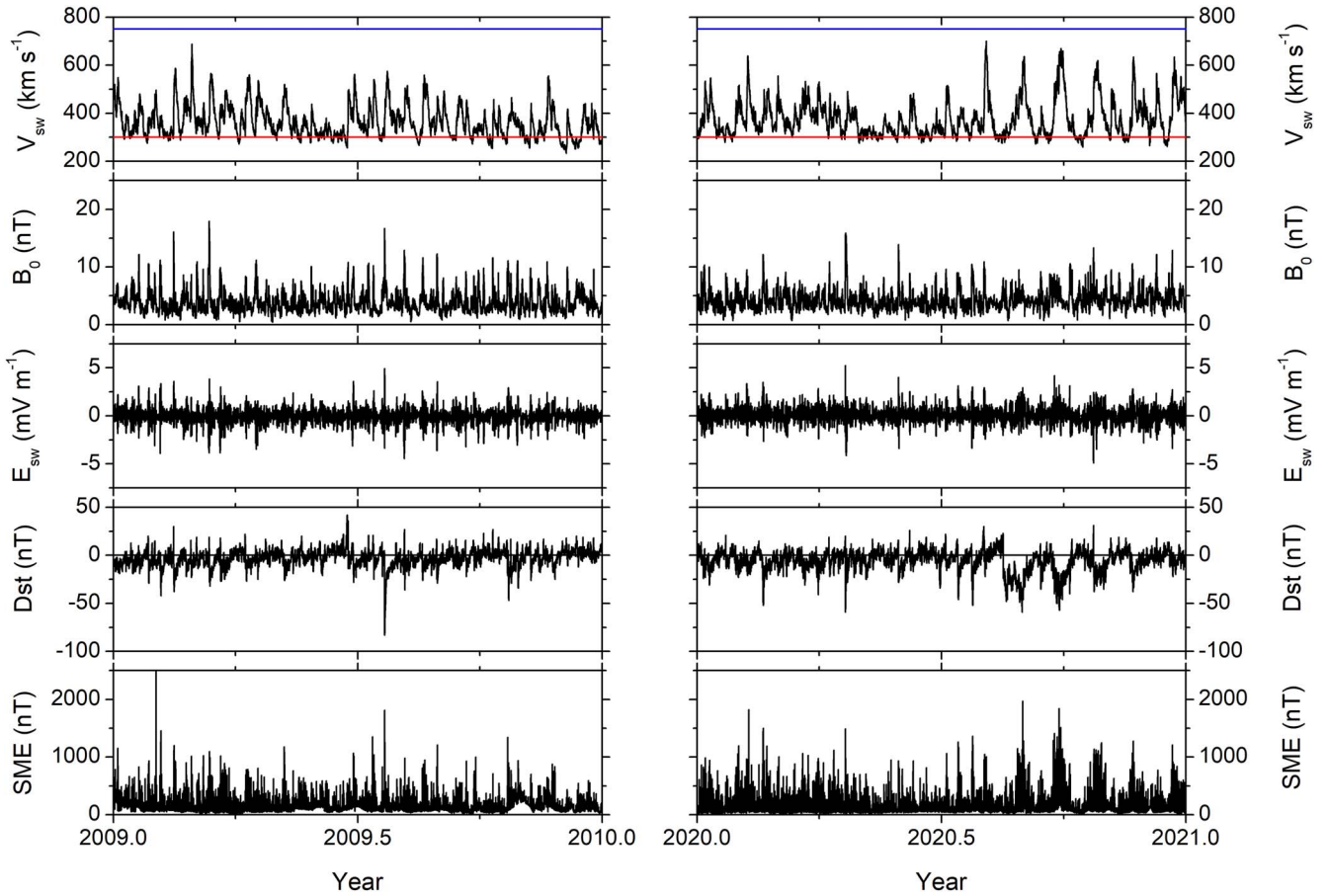


Figure 8. Two intervals of solar wind data and geomagnetic activity during solar minima are shown, the years 2009 and 2020. The panels are, from top to bottom: V_{sw} (km s^{-1}), B_0 (nT), E_{sw} (mV m^{-1}), Dst (nT), and SME (nT). SME data has been used in place of AE because AE data is not available for 2020. The blue and red horizontal lines in the V_{sw} panel indicate $V_{sw} = 750$ and 300 km s^{-1} , respectively.

ESSW events was $4.4 \pm 2.1 \text{ nT}$, a low value compared to the average B_0 for all solar wind events, $6.1 \pm 3.1 \text{ nT}$. The IMF negative B_z values are $-1.7 \pm 1.5 \text{ nT}$ compared to all negative B_z values of $-2.2 \pm 2.2 \text{ nT}$. The corresponding ESSW average AE value was $67 \pm 78 \text{ nT}$ (the 58 yr average for AE was $200 \pm 206 \text{ nT}$). the ESSW interval average Dst was $+2.2 \pm 9.9 \text{ nT}$ (the 58 yr average for Dst was $-14 \pm 22 \text{ nT}$). Thus, both AE and Dst during ESSW events are very low levels of geomagnetic activity. ESSW effects on the magnetosphere can thus be characterized as intervals of extreme geomagnetic quiet.

Why is geomagnetic activity extremely low during the ESSW events? The primary cause of geomagnetic activity is the magnetic reconnection between southward IMFs and the Earth's magnetopause magnetic fields (Dungey 1961; Tsurutani & Meng 1972). For large energy transfer between the solar wind and the magnetosphere (and resultant magnetic storms), the IMF must be intensely southward, have durations of hours or more (Tsurutani et al. 1990; Gonzalez et al. 1994). For ESSW events, none of these three conditions are met: B_z average negative values are low, ESSW events occur in regions where Alfvén waves are causing the high frequency B_z fluctuations, and the solar wind velocities, by definition, are extremely low.

HILDCAA events (Tsurutani & Gonzalez 1987; Hajra et al. 2013) have one out of three of these solar wind properties that cause magnetic storms. HILDCAAs are associated with high

$\sim 750\text{--}800 \text{ km s}^{-1}$ speeds, but are still dominated by the high frequency Alfvén waves. The negative B_z components of HILDCAAs are not intense (but more so than for ESSW events). Because HSSW/HILDCAA intervals occur for days (Hajra et al. 2013), the solar wind energy input into the magnetosphere is exceptionally large (Kozyra et al. 2006; Turner et al. 2006; Tsurutani et al. 2006b; Hajra et al. 2014). However, only intense and continuous substorms/DP2 events (enhanced AE/SME) occur and not magnetic storms (Tsurutani et al. 2006b; Hajra et al. 2013). Since ESSW events occur at the extreme trailing ends of HSSWs where super-radial expansion has weakened both the velocity and negative B_z fields, the resultant geomagnetic activity is much lower than HILDCAA intervals.

ESSW events with $V_{sw} < 300 \text{ km s}^{-1}$ have been detected with a relatively high frequency of occurrence during the last two solar cycles (SC23 and SC24). In these two cycles the number of events was 180 (84 and 96, respectively) while the number of events in SC21 and SC22 was 59 (37 and 22, respectively). The average duration of the events in the last two cycles was approximately the same for SC23-24 (~ 1.9 days for SC23; ~ 2.1 days for SC24) compared with those of SC21-22 (~ 2.5 days for SC21; ~ 1.8 days for SC22). Four of the five non-ICME sub-Alfvénic solar winds detected in Hajra & Tsurutani (2022) were ESSW events.

A possible cause of the higher number of ESSW events during the last two solar cycles can be noted in the $F_{10.7}$ solar

flux variations in Figure 1. With a decline in the solar activity, there was a decline in both the peak speeds of HSSs and the IMF intensity at 1 au (Tsurutani et al. 2011b). A similar feature was noted in interplanetary space at larger solar radial distances by the polar orbiting Ulysses spacecraft (McComas et al. 2013). In the solar minimum phase in between SC23 and SC24, coronal holes were located at heliographic midlatitudes (De Toma 2011) and the solar wind reaching the Earth had their peak speeds reduced by super-radial expansions (Tsurutani et al. 2011a).

Smith & Balogh (2008) (see also Janardhan et al. 2010; Raja et al. 2019) reported a weakening of open polar magnetic fields in the SC23 minimum. Smith and Balogh disputed the Svalgaard & Cliver (2007) argument that the minimum magnetic flux is invariant. Our observations of many low and midlatitude coronal holes during SC23 and SC24 (see also Luhmann et al. 2009) are in support of the Svalgaard and Cliver arguments. In fact, the average ESSW B_0 found in this study (4.4 ± 2.1 nT) is quite close to the Svalgaard and Cliver *floor* value of 4.6 nT. A scenario explaining the present results is a decrease in open polar magnetic fields is accompanied by low and midlatitude open magnetic fields (coronal holes).

Although SC23 has in the past been noted as having the most intense UV solar flare in recorded history (Tsurutani et al. 2005b) and the very intense Halloween magnetic storms (Mannucci et al. 2005), it is noteworthy that ESSW events were also present throughout this solar cycle (see Figure 2).

We examined the 10 lowest solar wind velocity events. These are shown in Appendix A. The four ESSW events shown in Figures 4 and 6 were representative of the 10 lowest speed ESSW events. ESSW events are the extreme ends of HSSW events and generally (but not always) have high C6+/C5+, O7+/O6+ ion charge state ratios and high Alfvénicities. The ESSW events had exceptionally high charge state ratios. This latter interesting feature is not understood at this time.

ESSW events were studied during solar maximum intervals. The results were the same, the ESSW events are associated with the extreme ends of HSSW intervals. There was no relationship between ESSW events and ICMEs or other types of solar/interplanetary phenomena found.

The proton temperatures in ESSW events were extremely low. The proton densities were higher than average values. Without doing detailed calculations, we suggest that the two parameters together lead to pressure balance in the expanding solar wind.

What is the relationship between the 1 au ESSW events reported here and the Sanchez-Diaz et al. (2016) VSSW events detected at 0.3 to 0.7 au? Sanchez-Diaz et al. detected high plasma density events (HPSSs) containing the HCSs in their VSSW events. They believe that the VSSW events were the interplanetary signatures of HCS crossings, e.g., the solar source is helmet streamers. Sanchez-Diaz et al. believe that VSSW events will not survive to 1 au distances. Our ESSW events detected at 1 au are characterized by high Alfvénicity and are located at the extreme ends of HSSW events, considerably different than the Sanchez-Diaz events. ESSW events certainly have coronal holes as their solar origins. ESSW events sometimes have the inclusion of HCSs and HPSSs, but they typically end the ESSW events rather than

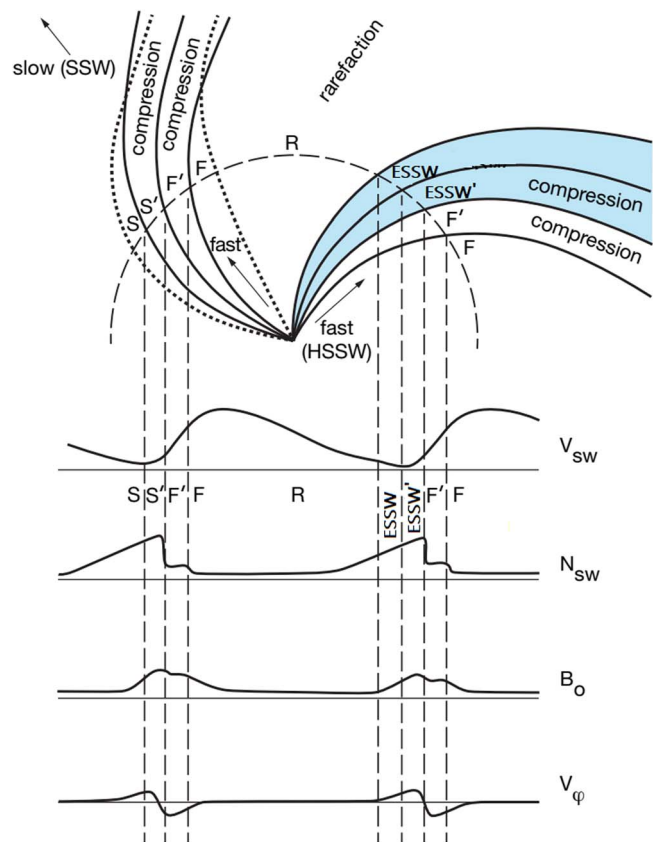


Figure 9. At the top is a schematic of two high-velocity (HSSW) streams and adjacent low-velocity (SSW) streams shown at one instant in time for a steady-state case. The dotted lines represent ideal spiral magnetic field lines and are also the flow lines for the steady-state flow in the corotating frame. The bottom curves show the changes in solar wind parameters as a function of time that will be observed by a spacecraft as the streaming pattern sweeps past. The top curve is V_{sw} , next is the ion density N_{sw} , then the magnetic field magnitude B_0 and at the bottom is the solar wind azimuthal velocity V_φ . S, S', F, and F' correspond to SSW, compressed SSW, HSSW, and compressed HSSW, respectively. The locations of the ESSW and the compressed ESSW (ESSW') are indicated in the top panel by the two blue shaded regions. This figure has been adapted from Belcher & Davis (1971).

being essential to them. We therefore think that VSSW and ESSW events are two separate phenomena.

Figure 9 gives a schematic summary of our present results. The figure shows two HSSW streams. These streams are designated in the figure as *fast* or “F” (as previously mentioned the names of the streams have changed with time). The SSW is designated as *slow* or “S”. As previously noted in Figure 5, the CIR that occurs at the antisunward edge of an HSSW is a double sheath region separated by a stream interface. The compressed ESSW is identified as the ESSW’ region. The compressed HSSW is identified as the F’ region. The stream interface is the discontinuity in the center of the CIR.

The ESSW region is indicated in the top schematic. The ESSW plasma parameters can be identified by the solar wind parameters shown in the lower part of the figure. The ESSW regions shown in blue are the extreme end of the HSSW rarefaction region and the first half of the CIR, the compressed ESSW or ESSW' region. The proportionate size of the ESSW interval to the much larger rarefaction region has been exaggerated for viewing. The ESSW' region is also much smaller than the ESSW region but has been exaggerated here for example.

5. Final Comments

Because there is such low geomagnetic activity during ESSW events, they could be useful for scientists to study the ground state of the magnetosphere and ionosphere. However, before doing such studies, the high plasma density CIR/HPS intervals should be removed from the analyses. These regions are only a small portion of the ESSW intervals as shown in Figures 4 and 6 and Appendix A (the proportion of the ESSW interval of the rarefaction region was exaggerated in Figure 9) and the deletion will not shorten the study interval in a substantial way. The high-density plasma impacts onto the magnetosphere/magnetotail can trigger very small substorms, much smaller than under ordinary solar wind conditions (Zhou & Tsurutani 2001; Tsurutani & Zhou 2003; Hajra & Tsurutani 2018b). This feature is of interest to the authors but will be postponed for further study.

We encourage interested scientists to study the ESSW events. A listing of all of the events is given in the Supporting Information for those interested in further detailed studies.

Data sources: (1) The interplanetary data were obtained from the NASA OMNI data center (https://spdf.gsfc.nasa.gov/pub/data/omni/low_res_omni/), (2) The solar wind ion charge state ratios were obtained from ACE SWICS (<http://www.srl.caltech.edu/ACE/ASC/level2/index.html>), (3) The Ulysses solar wind data were obtained from COHWeb (<https://omniweb.gsfc.nasa.gov/coho/>), (4) The polar coronal hole locations and extents were obtained from the National Solar Observatory homepage (<http://solis.nso.edu/vsm/>), (5) The geomagnetic activity indices were obtained from the World Data Center for Geomagnetism, Kyoto, Japan (<http://wdc.kugi.kyoto-u.ac.jp/>), (6) The SME data were obtained from SuperMAG (<https://supermag.jhuapl.edu/>), (7) The daily $F_{10.7}$ solar fluxes were obtained from the Laboratory for Atmospheric and Space Physics (LASP) Interactive Solar Irradiance

Data Center (<https://lasp.colorado.edu/lisird/>). B.T.T. wishes to acknowledge support from the International Space Science Institute for support of the ISSI International Team #455 on “Complex Systems Perspectives Pertaining to the Research of the Near-Earth Electromagnetic Environment.” Work of R.H. is funded by the Science and Engineering Research Board (SERB, grant No. SB/S2/RJN-080/2018), a statutory body of the Department of Science and Technology (DST), Government of India through the Ramanujan Fellowship. The authors declare no real or perceived financial conflicts of interests. The authors declare no conflict of interest with respect to the results of this paper.

Supporting Information

This supporting information gives a list (Table S1) of all ESSW events occurring between 1963 and 2021. Columns from left to right give the ESSW event number, ESSW event start year, day, hour, ESSW event end year, day, and hour.

Table S1
List of ESSW Events During 1963–2021

Number	Start Year	Start DOY	Start Hour	End Year	End DOY	End Hour
1	1963	331	12	1963	333	23
2	1963	344	3	1963	345	11
3	1963	351	0	1963	353	14
4	1963	360	15	1963	361	20

Note. Table S1 is published in its entirety in the electronic edition of the Astrophysical Journal. A portion is shown here for guidance regarding its form and content.

(This table is available in its entirety in machine-readable form.)

Appendix A

Appendix A shows the 10 lowest-speed ESSW events (Figure A1).

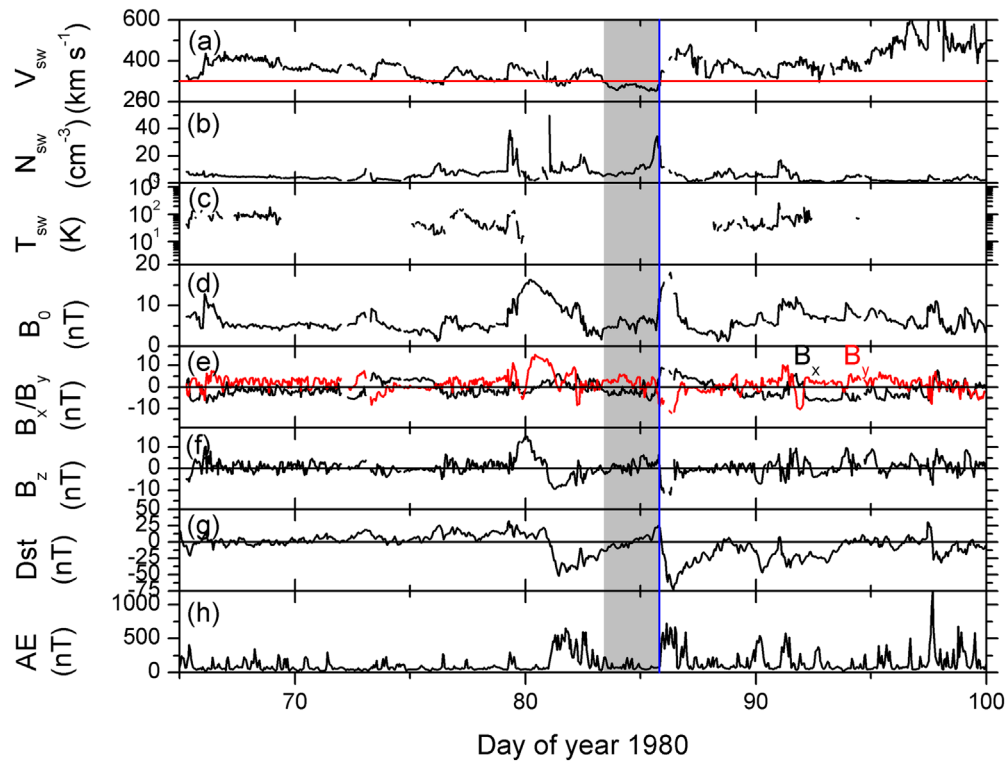


Figure A1. The ESSW event identified on days 83–85 in 1980. The panels from top to bottom are (a) V_{sw} (km s^{-1}), (b) N_{sw} (cm^{-3}), (c) T_{sw} (K), (d) IMF B_0 (nT), (e) B_x/B_y (nT), (f) B_z (nT), (g) Dst (nT), and (h) AE (nT). The red horizontal line in panel (a) corresponds to $V_{sw} = 300 \text{ km s}^{-1}$. The ESSW event is indicated by vertical shading. The complete figure set (seven images) is available in the online journal.

(The complete figure set (seven images) is available.)

Appendix B

Appendix B shows ESSW events (Figure B1) during the solar maxima, the years 2001 and 2013.

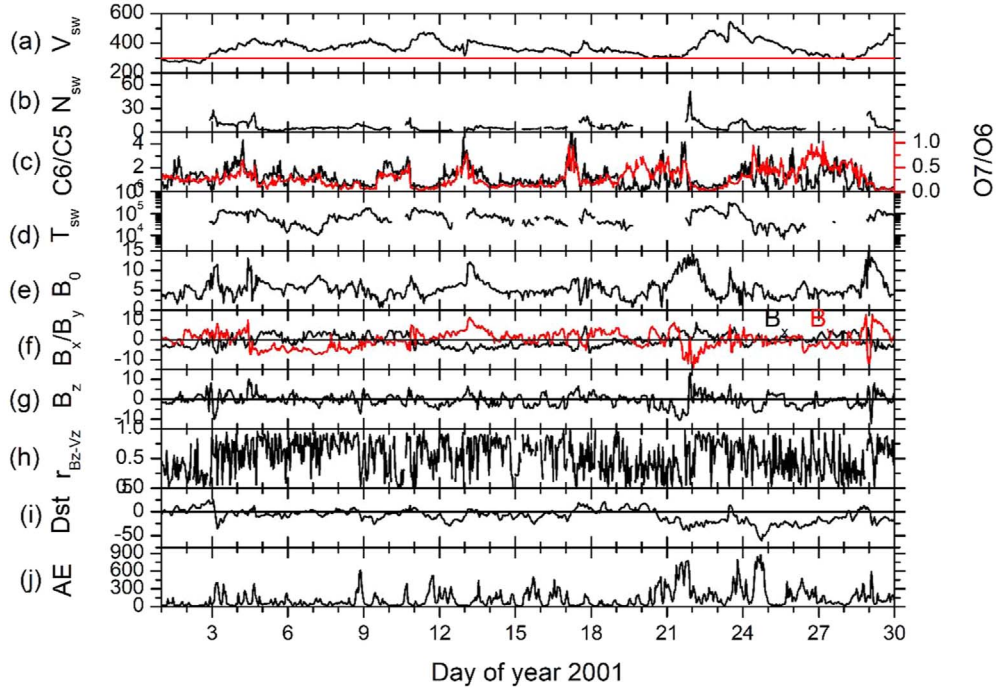


Figure B1. The solar wind and geomagnetic conditions during days 1–29 in 2001. The panels from top to bottom are (a) V_{sw} (km s^{-1}), (b) N_{sw} (cm^{-3}), (c) carbon and oxygen ion charge state ratios in the same panel, (d) T_{sw} (K), (e) IMF B_0 (nT), (f) B_x/B_y (nT), (g) B_z (nT), (h) B_z-V_z correlation coefficient, (i) Dst (nT), and (j) AE (nT). The red horizontal line in panel (a) corresponds to $V_{sw} = 300 \text{ km s}^{-1}$. The complete figure set (24 images) is available in the online journal.
(The complete figure set (24 images) is available.)

ORCID iDs

Rajkumar Hajra  <https://orcid.org/0000-0003-0447-1531>

References

- Abbo, L., Ofman, L., Antiochos, S. K., et al. 2016, *SSRv*, **201**, 55
- Akasofu, S.-I. 1964, *PSS*, **12**, 273
- Belcher, J. W., & Davis, L., Jr. 1971, *JGR*, **76**, 3534
- Carrington, R. C. 1859, *MNRAS*, **20**, 13
- Chapman, S., & Bartels, J. 1940, *Geomagnetism*, Vol. I (Oxford: Clarendon), 328
- Chen, P. F. 2011, *LRSP*, **8**, 1
- Cliver, E. W., Feynman, J., & Garrett, H. B. 1990, *JGR*, **95**, 17103
- D'Amicis, R., & Bruno, R. 2015, *ApJ*, **805**, 84
- D'Amicis, R., Perrone, D., Bruno, R., & Velli, M. 2021, *JGRA*, **126**, e28996
- De Toma, G. 2011, *SoPh*, **274**, 195
- Dungey, J. W. 1961, *PhRvL*, **6**, 47
- Echer, E., Gonzalez, W. D., & Tsurutani, B. T. 2008, *GeoRL*, **35**, L06S03
- Fisk, L. A., & Schwadron, N. A. 2001, *SSRv*, **97**, 21
- Gjerloev, J. W. 2009, *EOSTr*, **90**, 230
- Gonzalez, W. D., Joselyn, J. A., Kamide, Y., et al. 1994, *JGR*, **99**, 5771
- Gosling, J. T., Borini, G., Asbridge, J. R., et al. 1981, *JGR*, **86**, 5438
- Hajra, R., Echer, E., Tsurutani, B. T., & Gonzalez, W. D. 2013, *JGRA*, **118**, 5626
- Hajra, R., Echer, E., Tsurutani, B. T., & Gonzalez, W. D. 2014, *JGRA*, **119**, 2675
- Hajra, R., Tsurutani, B. T., Echer, E., Gonzalez, W. D., & Santolik, O. 2015, *ApJ*, **799**, 39
- Hajra, R., & Tsurutani, B. T. 2018a, in *Extreme Events in Geospace: Origins, Predictability, and Consequences*, ed. N. Buzulukova (Amsterdam: Elsevier), 373
- Hajra, R., & Tsurutani, B. T. 2018b, *ApJ*, **858**, 123
- Hajra, R., & Tsurutani, B. T. 2022, *ApJ*, **926**, 135
- Janardhan, P., Bisoi, S. K., & Gosain, S. 2010, *SoPh*, **267**, 267
- Kozyra, J. U., Crowley, G., Emery, B. A., et al. 2006, *GMS*, **167**, 319
- Krieger, A. S., Timothy, A. F., & Roelof, E. C. 1973, *SoPh*, **29**, 505
- Lakhina, G. S., Alex, S., Tsurutani, B. T., & Gonzalez, W. D. 2012, *GMS*, **196**, 267
- Lakhina, G. S., & Tsurutani, B. T. 2018, in *Extreme Events in Geospace: Origins, Predictability, and Consequences*, ed. N. Buzulukova (Amsterdam: Elsevier), 157
- Luhmann, J. G., Lee, C. O., Arge, C. N., et al. 2009, *SoPh*, **256**, 285
- Mannucci, A. J., Tsurutani, B. T., Iijima, B. A., et al. 2005, *GeoRL*, **32**, L12S02
- McComas, D. J., Angold, N., Elliott, H. A., et al. 2013, *ApJ*, **779**, 2
- McComas, D. J., Barraclough, B. L., Funsten, H. O., et al. 2000, *JGR*, **105**, 10419
- Meng, X., Tsurutani, B. T., & Mannucci, A. J. 2019, *JGRA*, **124**, 3926
- Neugebauer, M., & Snyder, C. W. 1966, *JGR*, **71**, 4469
- Nishida, A. 1968, *JGR*, **73**, 5549
- Phillips, J. L., Bame, S. J., Feldman, W. C., et al. 1995, *Sci*, **268**, 1030
- Press, W. H., Teukolsky, S. A., Vetterling, W. T., & Flannery, B. P. 1992, *Numerical Recipes: The Art of Scientific Computing* (2nd ed.; Cambridge: Cambridge Univ. Press)
- Raja, K. S., Janardhan, P., Bisoi, S. K., et al. 2019, *SoPh*, **294**, 123
- Sanchez-Diaz, E., Rouillard, A. P., Lavraud, B., et al. 2016, *JGRA*, **121**, 2830
- Sheeley, N. R., Jr., Harvey, J. W., Koomen, M. J., & Feldman, W. C. 1976, *SoPh*, **49**, 271
- Sheeley, N. R., Jr., Lee, D. D. H., Casto, K. P., Wang, Y. M., & Rich, N. B. 2009, *ApJ*, **694**, 1471
- Smith, E. J., & Balogh, A. 2008, *GeoRL*, **35**, L22103
- Smith, E. J., & Wolfe, J. H. 1976, *GeoRL*, **3**, 137
- Smith, E. J., Tsurutani, B. T., & Rosenberg, R. L. 1978, *JGR*, **83**, 717
- Suess, S. T., Ko, Y. K., Von Steiger, R., & Moore, R. L. 2009, *JGRA*, **114**, A04103
- Svalgaard, L., & Cliver, E. W. 2007, *ApJ*, **661**, L203
- Tang, F., Tsurutani, B. T., Gonzalez, W. D., Akasofu, S. I., & Smith, E. J. 2009, *JGR*, **94**, 3535
- Tsurutani, B. T., Echer, E., & Gonzalez, W. D. 2011a, *AnGeo*, **29**, 839
- Tsurutani, B. T., Echer, E., Guarnieri, F. L., & Gonzalez, W. D. 2011b, *JASTP*, **73**, 164
- Tsurutani, B. T., & Gonzalez, W. D. 1987, *P&SS*, **35**, 405
- Tsurutani, B. T., Gonzalez, W. D., Gonzalez, A. L. C., et al. 1995, *JGR*, **100**, 21717
- Tsurutani, B. T., Gonzalez, W. D., Gonzalez, A. L. C., et al. 2006a, *JGRA*, **111**, A07S01
- Tsurutani, B. T., Gonzalez, W. D., Guarnieri, F., et al. 2004a, *JASTP*, **66**, 167
- Tsurutani, B. T., Gonzalez, W. D., Lakhina, G. S., & Alex, S. 2003, *JGRA*, **108**, 1268
- Tsurutani, B. T., Gonzalez, W. D., Tang, F., et al. 1990, *P&SS*, **38**, 109
- Tsurutani, B. T., Gonzalez, W. D., Tang, F., & Lee, Y. T. 1992, *GeoRL*, **19**, 73
- Tsurutani, B. T., Gonzalez, W. D., Zhou, X. Y., Lepping, R. P., & Bothmer, V. 2004b, *JASTP*, **66**, 147
- Tsurutani, B. T., Hajra, R., Tanimori, T., et al. 2016, *JGRA*, **121**, 10130
- Tsurutani, B. T., Judge, D. L., Guarnieri, F. L., et al. 2005b, *GeoRL*, **32**, L03S09
- Tsurutani, B. T., & Lakhina, G. S. 2014, *GeoRL*, **41**, 287
- Tsurutani, B. T., Lakhina, G. S., Pickett, J. S., et al. 2005a, *NPGeo*, **12**, 321
- Tsurutani, B. T., Lakhina, G. S., Verkhoglyadova, O. P., et al. 2011c, *JASTP*, **73**, 5
- Tsurutani, B. T., McPherron, R. L., Gonzalez, W. D., et al. 2006b, *GMS*, **167**, 1
- Tsurutani, B. T., & Meng, C.-I. 1972, *JGR*, **77**, 2964
- Tsurutani, B. T., & Zhou, X.-Y. 2003, *AdSpR*, **31**, 1063
- Turner, N. E., Mitchell, E. J., Knipp, D. J., & Emery, B. A. 2006, *GMS*, **167**, 112
- von Steiger, R. 1996, in *AIP Conf. Proc. 382, Solar Wind Composition and Charge States* (Melville, NY: AIP), 193
- von Steiger, R., Schwadron, N. A., Fisk, L. A., et al. 2000, *JGR*, **105**, 27217
- Wang, Y. M., Grappin, R., Robbrecht, R., & Sheeley, N. R., Jr. 2012, *ApJ*, **749**, 182
- Winterhalter, D. E., Smith, E. J., Burton, M. E., Murphy, N., & McComas, D. J. 1994, *JGR*, **99**, 6667
- Zhou, X., & Tsurutani, B. T. 2001, *JGRA*, **106**, 18957